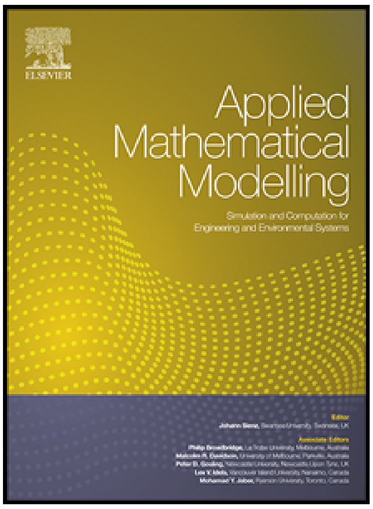

A solution approach for contact problems based on the dual interpolation boundary face method

Jianming Zhang, Xiaomin Shu, Jon Trevelyan, Weicheng Lin, Pengfei Chai

PII: S0307-904X(19)30090-3
DOI: https://doi.org/10.1016/j.apm.2019.02.013
Reference: APM 12666

To appear in: *Applied Mathematical Modelling*

Received date: 17 September 2018
Revised date: 27 January 2019
Accepted date: 6 February 2019

Please cite this article as: Jianming Zhang, Xiaomin Shu, Jon Trevelyan, Weicheng Lin, Pengfei Chai, A solution approach for contact problems based on the dual interpolation boundary face method, *Applied Mathematical Modelling* (2019), doi: https://doi.org/10.1016/j.apm.2019.02.013

Highlights

- A solution approach for contact problems based on the dual interpolation boundary face method is proposed.
- The solution approach is divided into outer and inner iterations.
- In the outer iteration, a contact boundary detection scheme is presented to determine the size of the contact zone.
- The inner iteration is only performed for frictional contact problems to determine whether the sliding occurs.
- The pressure oscillations near the contact boundary can be treated by the proposed approach.

A solution approach for contact problems based on the dual interpolation boundary face method

Jianming Zhang[a,*], Xiaomin Shu[a], Jon Trevelyan[b], Weicheng Lin[a], Pengfei Chai[a]

[a]*State Key Laboratory of Advanced Design and Manufacturing for Vehicle Body, Hunan University, Changsha, 410082 China*
[b]*Department of Engineering, Durham University, South Road, Durham DH1 3LE, UK*

Abstract

The recently proposed dual interpolation boundary face method (DiBFM) has been shown to have a much higher accuracy and improved convergence rates compared with the traditional boundary element method. In addition, the DiBFM has the ability to approximate both continuous and discontinuous fields, and this provides a way to approximate the discontinuous pressure at a contact boundary. This paper presents a solution approach for two dimensional frictionless and frictional contact problems based on the DiBFM. The solution approach is divided into outer and inner iterations. In the outer iteration, the size of the contact zone is determined. Then the elements near the contact boundary are updated to approximate the discontinuous pressure. The inner iteration is used to determine the contact state (sticking or sliding), and is only performed for frictional contact problems. To make the system of equations solvable, the contact constraints and some supplementary equations are also given. Several numerical examples demonstrate the validity and high accuracy of the proposed approach. Furthermore, due to the continuity of elements in DiBFM and the detection of the contact boundary, the pressure oscillations near the contact boundary can be treated.

Keywords: contact problems; dual interpolation boundary face method; contact boundary detection; weak discontinuity; contact constraints;

---

[*] Corresponding author
Email address: `zhangjianm@gmail.com` (Jianming Zhang)

supplementary equations.

---

1. Introduction

Contact problems are of great importance in engineering applications, such as gears, bearings, connecting rod and pin assemblies, etc. The solution to these problems based on the finite element method (FEM) and boundary element method (BEM) has long been an attractive research topic. In this paper, a solution approach based on the dual interpolation boundary face method (DiBFM) is presented.

The DiBFM was recently proposed by Zhang [1–3], and the method has been applied to thin-walled structures [4]. Like the Boundary Element Method (BEM), the method is also based on a boundary integral equation, but by using CAD geometries directly no geometric error will be introduced [5]. Compared with the interpolation accuracy of traditional discontinuous elements, the accuracy of dual interpolation elements is increased by two orders. In consequence, the method has been shown to deliver solutions of much higher accuracy, with improved convergence rates and computational efficiency for most cases [1, 2]. In addition, the method has an ability to naturally and accurately approximate both continuous and discontinuous fields. It is well known that the pressure from contact to non-contact region is discontinuous, and this motivates the present study to use the DiBFM to approximate the discontinuous pressure at contact boundary.

Schemes to accommodate the pressure discontinuity can be divided into weak discontinuity models and strong discontinuity models. In weak discontinuity models, the pressure is C^0 continuous at a contact boundary, while in the strong discontinuity models, a pressure jump exists at contact boundary. A strong discontinuity can be found, for example, when a flat punch comes into contact with an elastic plane, but these cases are readily addressed since the contact boundary is known *a priori*. For this type of problem, the use of discontinuous elements is an effective method as long as the contact boundary coincides with element endpoints. However, for general contact problems with an *a priori* unknown contact boundary, the contact pressure usually exhibits a weak discontinuity. We remark that where there is a discontinuous contact pressure, the integration accuracy can be difficult to ensure, potentially resulting in a loss of accuracy [6–9].

To address the weak discontinuity in contact pressure, two types of method are available: the mesh refining method [10] and the element updating method [9, 11, 12]. The mesh refining method is simple, but it is very costly and can become ineffective, especially when the contact boundary moves. The element updating method requires the calculation of the contact boundary. In [9, 13], the contact boundary was detected from variation in the normal gap between the contacting surfaces, since only the displacements form the independent variables in this penalty method. Conversely, in [12] the contact boundary was found from variation in the contact pressure. Alternatively, a bisection method may also be used to detect the contact boundary [14]. In the current paper, the element updating method is adopted to overcome the effect of the weak discontinuity in contact pressure. However, unlike [9, 12, 13], both the normal gap and contact pressure are used to detect the contact boundary. The normal gap is used when penetration between the two bodies is found, while the contact pressure is used when a tensile normal traction develops.

The proposed solution approach is divided into outer and inner iteration loops. In the outer iteration, the size of the contact zone is determined, and then the elements near the contact boundary are updated to approximate the discontinuous pressure. In the inner iteration, the contact state (sticking or sliding) is determined; this is performed only for frictional contact problems. To make the system of equations solvable, auxiliary equations are required and these are provided by the contact constraint equations and some supplementary equations. Numerical examples, without and with friction, are presented to demonstrate the validity and high accuracy of the proposed approach. In addition, due to the continuity of the S1 element and the detection of the contact boundary, the pressure oscillations near the contact boundary can be avoided in the proposed approach.

2. A brief introduction of DiBFM

In the DiBFM [1, 2], the elements are called dual interpolation elements. The elements are composed of a combination of source and virtual nodes. However, the boundary integral equations are collocated only at the source nodes. That is to say, the virtual nodes are not used as collocation points. As a result, the number of linear equations after discretisation is less than the number of unknown quantities. In order to arrive at a square linear system, the degrees of freedom relating to all virtual nodes need to be condensed and this can be achieved by considering additional constraint equations.

In this section, the element in DiBFM is introduced, and the method (the second-layer interpolation) to condense the degrees of freedom of virtual nodes will be presented.

2.1. The element in DiBFM

As shown in Figure 1, the nodes of a dual interpolation element are divided into two groups: source and virtual nodes. Ignoring virtual nodes, it becomes a traditional discontinuous boundary element. When both the virtual nodes and the source nodes are taken into account, it is equivalent to a standard continuous element. In this way, the dual interpolation element is able to unify the traditional continuous and discontinuous element approaches. As shown in the Figure, we identify the elements with the notation S1, S2, S3 indicating the number of source nodes. This notation derives from the fact that the degrees of freedom relating to the virtual nodes are condensed and in DiBFM they do not form part of the final linear system being solved.

The addition of the two virtual nodes in these elements means that, in comparison with the order of interpolation function of the traditional discontinuous elements using the source nodes alone, the interpolation in the dual interpolation elements is increased by two orders. This leads to a considerable improvement in accuracy [1].

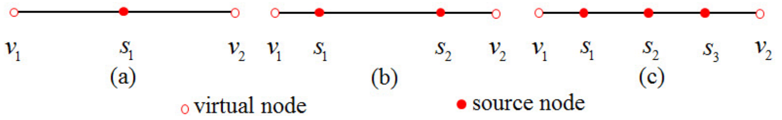

Figure 1: Dual interpolation elements in 2D problems: (a) S1, (b) S2, and (c) S3.

2.2. The first-layer interpolation

The first-layer interpolation is similar to the interpolation in a traditional continuous boundary element. The difference is that shape functions relating to both source nodes and virtual nodes are used, so that in interpolating an arbitrary quantity φ we write

$$\varphi(\xi) = \sum_{\alpha=1}^{n\alpha} N_\alpha^s(\xi)\varphi(Q_\alpha^s) + \sum_{\beta=1}^{n\beta} N_\beta^v(\xi)\varphi(Q_\beta^v) \tag{1}$$

where $N_\alpha^s(\xi)$ is the shape function of the α^{th} source node, $N_\beta^v(\xi)$ is the shape function of the β^{th} virtual node, $\varphi(Q_\alpha^s)$ is the nodal value of the α^{th} source node, and $\varphi(Q_\beta^v)$ is the nodal value of the β^{th} virtual node. $n\alpha$ and $n\beta$ are the total number of source and virtual nodes belonging to the dual interpolation element, respectively, and $\xi \in [-1, 1]$ is the usual local parametric coordinate. In DiBFM, the virtual nodal value $\varphi(Q_\beta^v)$ is not an independent variable, and its relation to the value of φ at the source nodes is determined by the second-layer interpolation.

It should be noted that the shape functions $N_\alpha^s(\xi)$ and $N_\beta^v(\xi)$ in equation (1) are the Lagrange polynomials one would use in a conventional element having a number of nodes equal to $(n\alpha + n\beta)$. For the S1 element shown in Figure 1(a), then, these would be the standard continuous quadratic shape functions $N_1^v(\xi) = -0.5\xi(1-\xi), N_1^s(\xi) = (1-\xi)(1+\xi), N_2^v(\xi) = 0.5\xi(1+\xi)$. Shape functions for the other cases are provided in [1].

2.3. The second-layer interpolation

The second-layer interpolation is used to construct the relationships between source nodes and virtual nodes. These relationships can then be used to condense the degrees of freedom of the virtual nodes. The second-layer interpolation can be used to approximate both continuous and discontinuous fields.

2.3.1. The moving least square approximation

In this paper, the second-layer interpolation is constructed by the moving least square (MLS) approximation. In our implementation, the MLS is employed only to construct the relationships between source and virtual nodes, rather than evaluate the shape functions at each Gauss point in the boundary integration. The virtual nodal value can be approximated by the MLS as

$$\varphi(Q_\beta^v) = \sum_{m=1}^{M} \psi_m^{vs}(\eta_\beta^v)\varphi(Q_m^s) \tag{2}$$

where M is the total number of source nodes Q_m^s located in the influence domain of the virtual node Q_β^v. The term $\psi_m^{vs}(\eta_\beta^v)$ is the MLS shape function corresponding to source node Q_m^s, and η_β^v is the parametric coordinate of virtual node Q_β^v. This coordinate is used to locate a point on a curve or straight line, and its value $\eta \in [0, 1]$. The derivation of equation (2) can be found in [15].

2.3.2. Approximation of continuous and discontinuous fields

The continuous or discontinuous behaviour at an element end point can be accommodated by simply placing either one or two virtual nodes at the point. Two virtual nodes are used when approximating a discontinuous field, while only one virtual node is used when modelling a continuous function. By manipulating the influence domains of each virtual node, the continuous or discontinuous fields can be naturally and accurately approximated. To illustrate this feature, a schematic diagram is shown in Figure 2.

For discontinuous fields, two virtual nodes v_0 and v_1 are placed at the discontinuous boundary, as in Figure 2(a). In the figure, the influence domain of v_0 covers only the three blue source nodes; while the influence domain of v_1 covers only the three red source nodes. Due to these different influence domains, when using the second-layer interpolation (2) the nodal values at v_0 and v_1 are different, allowing discontinuous behaviour.

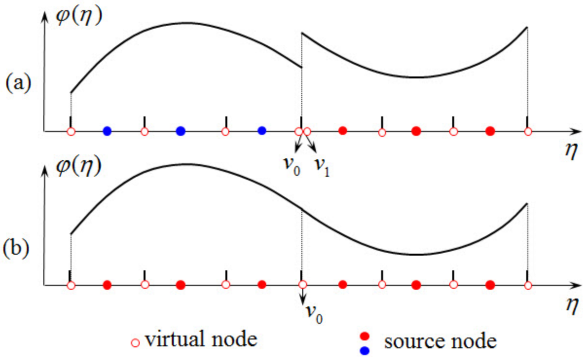

Figure 2: Approximation the continuous or discontinuous fields

For the modelling of continuous fields, only a single virtual node, v_0, is placed at the element end point, as shown in Figure 2(b). The domain of influence of this virtual node in the second-layer interpolation (2) spans both elements to which it belongs. In this way a continuous approximation is achieved.

In summary, by manipulating the influence domains of virtual node in the second-layer interpolation, both continuous and discontinuous fields can be naturally and accurately approximated.

2.4. The boundary integral equation

We consider an elastic body ocupying domain $\Omega \subset \mathbb{R}^2$, having boundary $\partial\Omega \equiv \Gamma$. In the absence of body forces, the boundary integral equation [16] can be written in the following form for each body

$$c_{ij}(P)u_j(P) = \int_\Gamma U_{ij}(P,Q)t_j(Q)d\Gamma(Q) - \int_\Gamma T_{ij}(P,Q)u_j(Q)d\Gamma(Q), \quad P,Q \in \Gamma \tag{3}$$

where u_j and $t_j (j = 1, 2)$ are the displacement and traction components, respectively, and U_{ij}, T_{ij} are the displacement and traction kernels, or fundamental solutions. $c_{ij}(P)$ is the coefficient matrix of the jump term that arises from the strongly singular nature of the integral containing the traction kernel. For 2D plane-strain problems:

$$U_{ij}(P,Q) = \frac{1}{8\pi G(1-\nu)}\left[(3-4\nu)\delta_{ij}\ln\frac{1}{r} + r_{,i}r_{,j}\right] \tag{4}$$

$$T_{ij}(P,Q) = -\frac{1}{4\pi(1-\nu)r}\left\{\frac{\partial r}{\partial n}\left[(1-2\nu)\delta_{ij} + 2r_{,i}r_{,j}\right] - (1-2\nu)(r_{,i}n_j - r_{,j}n_i)\right\} \tag{5}$$

where r is the distance between the source node P and the field point Q, n is the outward normal at point Q, and G and ν are the shear modulus and Poisson's ratio, respectively.

3. Frictional Contact problems

3.1. Local contact coordinate system

Consider a node pair, a and b, on the boundaries of two contacting bodies A and B, as in Figure 3. The common normal for nodes in the contact zone is defined as follows:

$$n = \mathbf{n}_{AB} = \frac{\mathbf{n}_A E_A - \mathbf{n}_\mathbf{B} E_B}{||\mathbf{n}_A E_A - \mathbf{n}_\mathbf{B} E_B||} \tag{6}$$

Here E denotes the Young's modulus of the body indicated by its subscript. The tangential direction τ is obtained simply by rotating n through 90°. The contact node pair is determined by the closest point projection. In this paper, the nodes on the less rigid body are projected onto the other contacting body. The normal direction of the more rigid solid is used to determine the closest point. The common normal is only used to define the normal direction of the displacement and traction, and it is not used to determine the closest point.

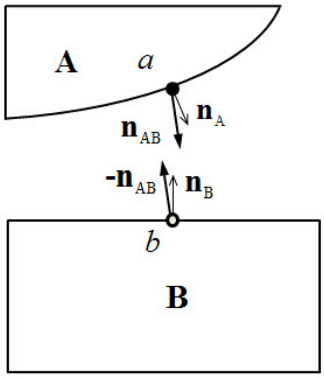

Figure 3: Definition of the common contact direction

3.2. Coulomb friction law

The Coulomb friction law defines a limitation for the tangential traction in the contact zone. The limitation can be written as

$$|t_\tau| \leq \mu \, |t_n| \tag{7}$$

where μ is the coefficient of friction, t_τ is the tangential traction and t_n is the normal traction. As long as the tangential traction is sufficiently small that equation (7) is satisfied, the contacting surfaces will stick to each other. Otherwise, sliding will occur with tangential traction $|t_\tau| = \mu \, |t_n|$ applying in a direction opposing the relative motion.

3.3. Contact constraint equations

For any collocation node in the non-contact zone, there are two unknown variables and two integral equations (Equation (3) for $i = 1, 2$). However, for any collocation node in the contact zone, there are four unknown variables, both tractions and displacements being unknown, but only two integral equations. Contact constraints will be imposed to provide the required number of auxiliary equations to reach a solvable, square system. The contact constraint equations for both frictional and frictionless are presented below.

3.3.1. Frictional contact constraint equations

The contact constraints depend on the contact state. Since the actual contact zone is unknown *a priori*, we start with a contact zone larger than the actual contact zone. Then the contact state for any node pair can be classified into three types: non-contact, sticking and sliding. The constraints are given below for these three contact states. Besides, it should be noted that the node-to-node contact scheme is adopted in this paper.

In the non-contact state, both surfaces are traction free. Since the load is applied incrementally in solving the non-linear frictional contact problem, the traction is expressed as that from the previous load step plus the incremental traction in the current load step. The constraint equations for the contact node pairs on bodies A and B can therefore be written as:

$$t_n^A + \Delta t_n^A = 0; \quad t_\tau^A + \Delta t_\tau^A = 0 \tag{8}$$

$$t_n^B + \Delta t_n^B = 0; \quad t_\tau^B + \Delta t_\tau^B = 0 \tag{9}$$

In the sticking state, the normal gap and the tangential relative displacement are zero, and the traction is the same on the two bodies A and B. The constraints for the contact node pairs on bodies A and B can therefore be written as:

$$\Delta u_n^A = g - \Delta u_n^B; \quad \Delta u_\tau^A = \Delta u_\tau^B \tag{10}$$

$$t_n^B + \Delta t_n^B = t_n^A + \Delta t_n^A; \quad t_\tau^B + \Delta t_\tau^B = t_\tau^A + \Delta t_\tau^A \tag{11}$$

In the sliding state, the normal gap is also zero, and the tangential traction is equal to the frictional coefficient multiplied by the normal traction. Again, the traction is the same on the two bodies A and B. The constraints for the contact node pairs on bodies A and B can therefore be written as:

$$\Delta u_n^A = g - \Delta u_n^B; \quad t_\tau^A + \Delta t_\tau^A = \pm\mu\left(t_n^B + \Delta t_n^B\right) \tag{12}$$

$$t_n^B + \Delta t_n^B = t_n^A + \Delta t_n^A; \quad t_\tau^B + \Delta t_\tau^B = t_\tau^A + \Delta t_\tau^A \tag{13}$$

In Equations (8)-(13), Δu_j and Δt_j are the incremental changes in displacements and tractions, due to the current incremental load step; u_j and t_j are the total displacements and tractions before the current load step. The superscript A and B denotes the corresponding contacting body. g denotes the normal gap at the current load step, and should be updated after each load step. The definitions of n and τ can be seen in Section 3.1.

3.3.2. Frictionless contact constraint equations

In frictionless contact, only non-contact and sliding states can exist. For the non-contact state, the non-contact constraint equations (8) and (9) still hold. For the sliding state, the constraint Equation (13) also holds, but the constraint Equation (12) needs to be rewritten as

$$\Delta u_n^A = g - \Delta u_n^B; \quad t_\tau^A + \Delta t_\tau^A = 0. \tag{14}$$

3.4. Supplementary equations for a virtual node in the contact zone

Unlike solving a potential problem or more straightforward elasticity problems, the consideration of contact means that not all degrees of freedom of virtual nodes are condensed by the second-layer interpolation. In a contact problem, whether the node is a source node or a virtual node, the contact constraints are required to be satisfied. To impose the constraints, the degrees of freedom relating to the virtual nodes in the potential contact zone are not condensed, but will be additional system unknowns. As presented in Section 2, the virtual nodes are not used as collocation nodes. Thus, the two integral equations of the form (3) have not been established, and two auxiliary equations are required. To provide these equations, the second-layer interpolation (2) is employed.

3.4.1. Cross-constraint scheme to construct supplementary equations

In the potential contact zone, the displacement and the traction are both unknown quantities. Then a question is which one requires the second-layer interpolation to construct the supplementary equations. In this paper, a cross-constraint scheme is used to construct these equations.

The cross-constraint scheme can be described as follows: if the virtual nodal normal or tangential traction is a contact constraint, then the second-layer interpolation of the normal or tangential displacement will be used as a supplementary equation. In contrast, if the virtual nodal normal or tangential displacement is a contact constraint, then the second-layer interpolation of the normal or tangential traction will be used as a supplementary equation.

For frictionless and frictional contact problems, there are a total of three different contact states (non-contact, sticking and sliding). Thus, the supplementary equations are also different. The following summarizes the supplementary equations for different contact states.

3.4.2. Supplementary equations for different contact states

In the non-contact state, both the normal and tangential traction contact constraints for body A are imposed; see equation (8). Thus, the second-layer interpolation of the normal and tangential displacement is used as the supplementary equations as below:

$$\Delta u_d(Q^v_\beta)^A = d_i \left\{ \sum_{m=1}^{M} \psi^{vs}_m(\eta^v_\beta)\Delta u_i(Q^s_m)^A \right\}; \quad d=(n,\tau), i=(x,y). \tag{15}$$

In the sticking state, both the normal and tangential displacement contact constraints for body A are imposed; see equation (10). Thus, the second-layer interpolation of the normal and tangential traction is used as the supplementary equations as below:

$$(t_d + \Delta t_d)(Q^v_\beta)^A = d_i \left\{ \sum_{m=1}^{M} \psi^{vs}_m(\eta^v_\beta)(t_i + \Delta t_i)(Q^s_m)^A \right\}; \quad d=(n,\tau), i=(x,y). \tag{16}$$

In the sliding state, for body A, the normal displacement and tangential traction constraints are imposed; see equations (12) and (14). Thus, the second-layer interpolation of normal traction and tangential displacement constraints are used as the supplementary equations. The two supplementary equations for virtual node on body A are:

$$(t_n + \Delta t_n)\,(Q^v_\beta)^A = n_i \left\{ \sum_{m=1}^{M} \psi^{vs}_m(\eta^v_\beta)\,(t_i + \Delta t_i)\,(Q^s_m)^A \right\}; \quad i=(x,y); \tag{17a}$$

$$\Delta u_\tau(Q^v_\beta)^A = \tau_i \left\{ \sum_{m=1}^{M} \psi^{vs}_m(\eta^v_\beta)\Delta u_i(Q^s_m)^A \right\}; \quad i=(x,y). \tag{17b}$$

For nodes on body B, both the normal and tangential traction contact constraints are always imposed; see equations (9), (11) and (13). Thus, the equations for the second-layer interpolation of the normal and tangential displacement are used as the supplementary equations. The two supplementary equations for virtual node on body B are:

$$\Delta u_d(Q^v_\beta)^B = d_i \left\{ \sum_{m=1}^{M} \psi^{vs}_m(\eta^v_\beta)\Delta u_i(Q^s_m)^B \right\}; \quad d=(n,\tau), i=(x,y). \tag{18}$$

In the above, d_i is the direction cosine and the Einstein summation convention is used. Further, $\Delta\varphi_d(Q^v_\beta) = d_x\Delta\varphi_x(Q^v_\beta) + d_y\Delta\varphi_y(Q^v_\beta), \varphi = (u, t), d = (n, \tau)$. The definitions of the variables are the same as those defined in Section 2.3.1 and Section 3.3.

4. Updating the elements near the contact boundary

4.1. Contact boundary detection method

At any stage in the analysis, the size of the contact zone is changed according to the results of the analysis, progressively refining towards the true contact zone. The current estimate of the contact zone may be larger or smaller than the real contact zone, and the contact boundary detection method used to identify the size of the contact zone for the next iteration is different depending on whether the size is currently overestimated or underestimated. In this section we present the method of detecting the contact boundary in both cases.

If the potential contact zone is larger than the real contact zone, after computation a tensile normal traction will develop, which violates a physical constraint. In this case, all elements are interrogated to identify the element in which the contact pressure (normal traction) is partially negative and partially positive. This element is named the contact boundary element. The updated location of the contact boundary is found by linear interpolation between the two nodes on the contact boundary element having normal tractions closest to $t_n = 0$, one node having a positive normal traction, the other being negative. The scheme is illustrated in Figure 4.

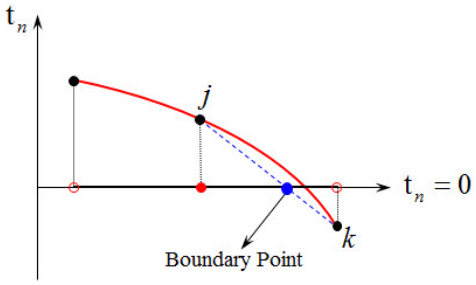

Figure 4: Boundary detection method in contact boundary element

In Figure 4, the interpolation considers nodes j and k being the two nodes having a normal traction closest to $t_n = 0$. Let us consider, without loss of generality, the case $t_n(j) > 0$ and $t_n(k) < 0$, in which case the location of the contact boundary can be estimated as

$$\bar{x} = x(j) + \frac{t_n(j)}{t_n(j) - t_n(k)} \left[x(k) - x(j) \right]. \tag{19}$$

In the above equation, x can be the Cartesian coordinate or the parametric coordinate as required.

A very similar method can be used to locate the contact boundary when the potential contact zone is smaller than the real contact zone. In this case, at the current step in the analysis penetration is predicted to occur, also violating a physical constraint. Here, we find the element where the normal gap is partially negative and partially positive and, using the normal gap to replace the pressure, the linear interpolation (19) can be performed again to determine the contact boundary.

The contact boundary detection repeats until no tensile normal tractions occur, and no penetration occurs, at any nodes.

4.2. Updating the elements near the contact boundary

In our implementation, the elements near the contact boundary are updated to approximate the traction, which is allowed to become discontinuous. A fine mesh can be obtained at the contact boundary, which is more conducive to the accurate approximation of discontinuous traction. This method differs from that used in [9, 11, 12], in which the authors moved the adjacent node to the contact boundary. To illustrate our method, a schematic diagram is shown in Figure 5.

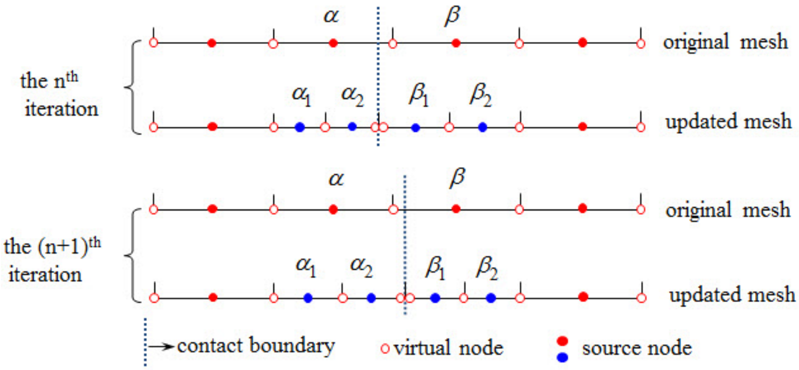

Figure 5: Updating the elements near the contact boundary

In this Figure, the adjacent elements at the contact boundary are the elements labelled α and β. The two elements are divided into four sub-elements $\alpha_1, \alpha_2, \beta_1$ and β_2, and two virtual nodes are placed at the contact boundary to model the discontinuous traction. Using this approach, each update of the mesh near the contact boundary causes the total number of elements to increase by two.

It should be noted that the final contact boundary is determined when no normal tension and no penetration occur, and this usually requires multiple iterations. If the number of elements increases with each iteration, a very dense mesh may be obtained, which is unnecessarily detrimental to computational efficiency.

To avoid the above problem, in our implementation, there are two types of mesh: the original mesh and the updated mesh. In each iteration, having located the new estimate of the contact boundary, we go back to the original mesh to generate the updated mesh, as shown in Figure 5. Using this algorithm, the size of the model does not increase with each iteration and the calculation proceeds efficiently.

4.3. The solution approach for contact problems

The solution approach based on the DiBFM is summarized in Figure 6. Loop 1 is the outer iteration, which is used to determine the size of the contact zone. Loop 2 is the inner iteration, which is employed to determine the contact state. The inner iteration is performed only for frictional contact problems. For frictional contact problems, also, the load is applied in increments to arrive at the correct contact area. We adopt the conditions for convergence from [17–21].

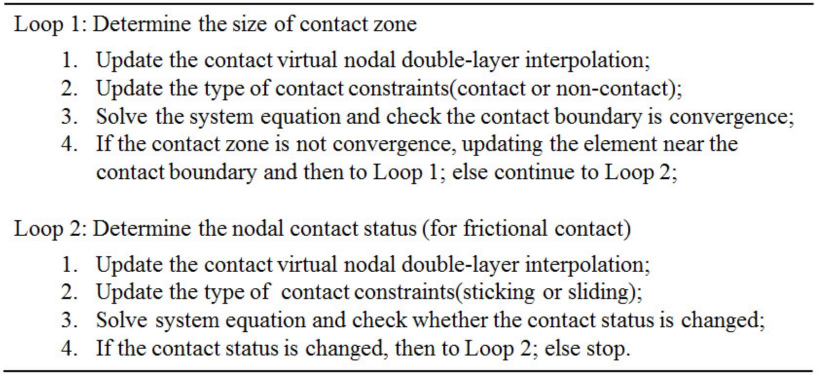

Loop 1: Determine the size of contact zone

1. Update the contact virtual nodal double-layer interpolation;
2. Update the type of contact constraints(contact or non-contact);
3. Solve the system equation and check the contact boundary is convergence;
4. If the contact zone is not convergence, updating the element near the contact boundary and then to Loop 1; else continue to Loop 2;

Loop 2: Determine the nodal contact status (for frictional contact)

1. Update the contact virtual nodal double-layer interpolation;
2. Update the type of contact constraints(sticking or sliding);
3. Solve system equation and check whether the contact status is changed;
4. If the contact status is changed, then to Loop 2; else stop.

Figure 6: The solution approach for contact problems based on the DiBFM

5. Numerical examples

In this section, three examples are presented. S1 elements will be used in all examples in which the DiBFM is used. The first example, Hertzian contact, has an analytical solution, and this is used to demonstrate that the S1 element in the proposed approach can achieve the accuracy obtained by the traditional discontinuous quadratic element. Besides, due to the continuity of the S1 element and the detection of the contact boundary, the pressure oscillations near the contact boundary can be treated. The other two examples (with two and three contact zones) demonstrate further the above advantages of the proposed approach on problems having different characters.

5.1. Hertzian contact problem

In the first example we consider an elastic cylinder coming into contact with a rigid plate. The geometry, material properties, loads and boundary conditions are shown in Figure 7(a). A very small load, $p = 0.4$, has been chosen to give small displacements in order to match closely the assumption of small deformation in the analytical solution [22], according to which the contact half-width, b, is

$$b = 2\sqrt{\frac{2R^2p(1-\nu^2)}{E\pi}}, \tag{20}$$

and the distribution of the normal contact pressure, p_n, is

$$p_n = \frac{4Rp}{\pi b^2}\sqrt{(b^2 - x^2)}. \tag{21}$$

For the given set of parameters, the contact half-width $b = 0.54462$.

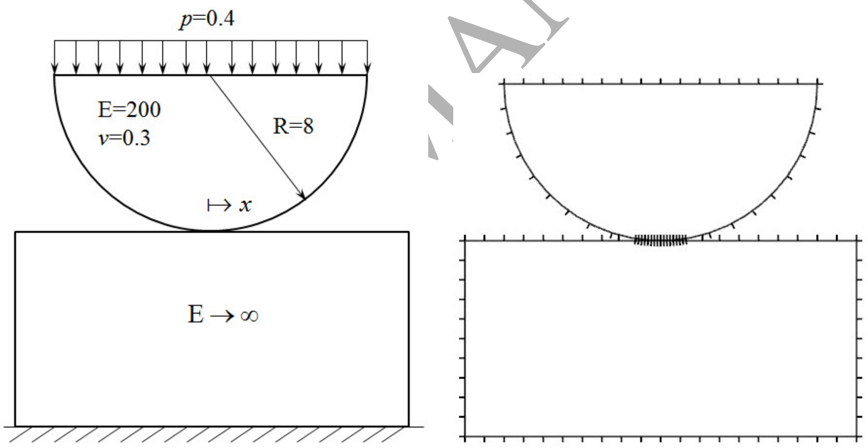

(a) Computational model (b) Computational mesh

Figure 7: Frictionless Hertzian contact

5.1.1. Comparison with the analytical solution

The contact pressure and the contact half-width are respectively shown in Figure 8 and in Table 1, and three sets of results (h1, h2 and h3) are presented. The three sets of results correspond to different meshes used in the potential contact zone ($-1.276 < x < 1.276$), but the mesh in all non-contact regions remains unchanged throughout. The initial number of elements in the potential contact zone is 16 (mesh h1), 24 (mesh h2) and 32 (mesh h3).The mesh in the non-contact zone can be seen in Figure 7(b).

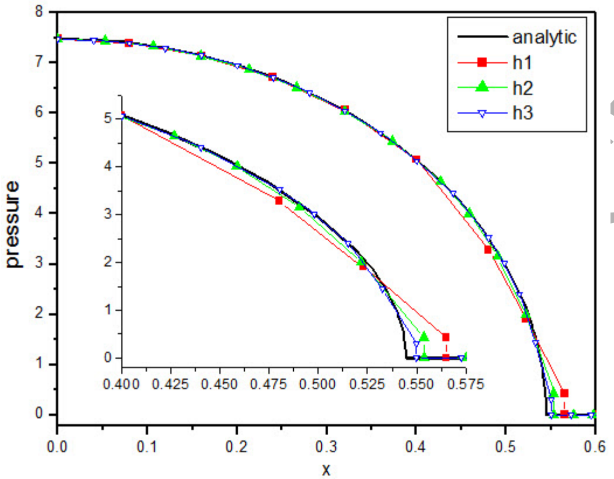

Figure 8: Contact pressure solutions, from different meshes, in the potential contact zone

Table 1: Contact half-width for different mesh

mesh size	b^*	error $= \left\|\frac{b^*-b}{b}\right\|$
h1	0.56511	3.76%
h2	0.55357	1.64%
h3	0.54991	0.94%

From Figure 8, it can be seen that with increasing mesh density in the potential contact zone, the contact pressure becomes almost coincident with the analytical solution; this provides a graphical demonstration of the convergence of the proposed approach. Similarly, Table 1 shows the convergence in terms of the error in the contact half-width (here b^* denotes the numerical approximation to the contact half-width, and b is the analytical solution). These results demonstrate the validity of the proposed approach, including its ability to predict the correct extent of the contact region.

5.1.2. *Comparison with traditional discontinuous elements*

Figures 9 and 10 show comparisons with traditional discontinuous boundary elements for this Hertzian contact problem. In the figures, the initial number of elements in the potential contact zone is equal for both methods (mesh h3). In the traditional method, no contact boundary detection has been performed. We compare against both traditional constant (Figure 9) and discontinuous quadratic element (Figure 10) since (i) the constant elements have the same number of source nodes as the S1 element in our DiBFM analysis, and (ii) the quadratic elements will have the same underlying order of variation of the displacements and tractions over the element.

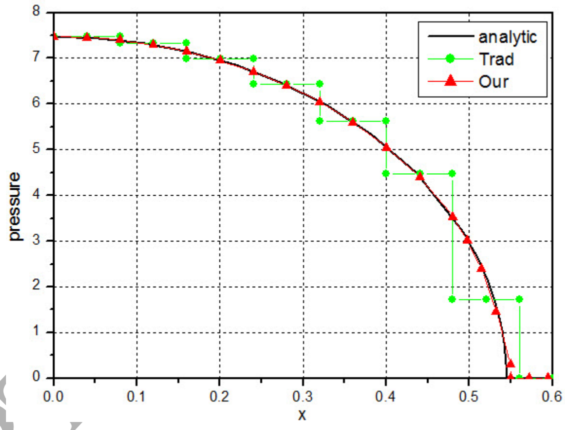

Figure 9: Contact pressure: comparison against traditional constant elements

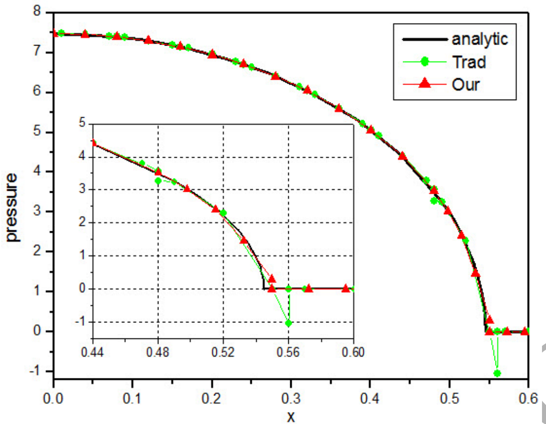

Figure 10: Contact pressure: comparison against traditional discontinuous quadratic elements

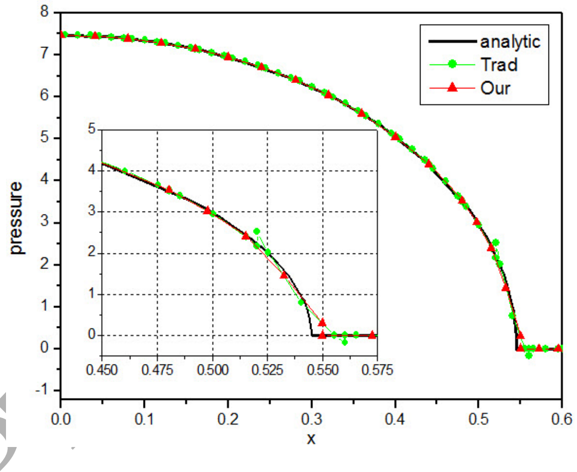

Figure 11: Contact pressure: comparison against refined traditional discontinuous quadratic elements

From Figure 9, it can be seen that the accuracy of our proposed approach (Our) is considerably higher than the traditional constant element (Trad). Figure 10 shows that the result of our proposed approach (Our) is almost consistent with that of the traditional discontinuous quadratic element (Trad). However, obvious pressure oscillations near the contact boundary can be seen in this element (Trad). This is due to the fact that (i) the discontinuous element is used and (ii) the contact boundary is usually in an element, not at the endpoint of the element, which reduces the regularity of the solution [9]. In contrast, the S1 element in DiBFM is a continuous element. Furthermore, due to the contact boundary detection, the contact boundary is at the endpoint of the element. Thus, our proposed approach (Our) provides a higher fidelity solution near the contact boundary than the traditional discontinuous quadratic element (Trad). Even if the mesh size of the potential contact zone is halved for traditional discontinuous quadratic element (Trad), this conclusion still holds, see Figure 11.

This study shows that the S1 element in DiBFM can achieve the accuracy obtained by the traditional discontinuous quadratic element, which proves the high accuracy of the proposed approach. In addition, due to the continuity of the S1 element and the detection of the contact boundary, the pressure oscillations near the contact boundary can be treated in our method.

5.2. A flat rounded punch

In this example, an elastic flat rounded punch comes into contact with an elastic foundation. The geometry, loads and boundary conditions are shown in Figure 12(a). The material properties of the punch and the foundation are equal, both having Young's modulus $E = 200$ GPa and Poisson's ratio $\nu = 0.3$. The example has been solved in [23], and a sharp increase in pressure is seen to occur at the intersection of the line and the arc. To capture this large pressure gradient, a fine mesh is used near the intersection. We use 20 elements in $(0 < x < 44.5)$, 10 elements in $(44.5 < x < 45.0)$ and 25 elements in $(45 < x < 45.27)$, and the mesh in the non-contact zone can be seen in Figure 12(b). The results of the traditional discontinuous quadratic element are used for comparison, and the S1 element in DiBFM is again adopted in the proposed approach. Both frictionless and frictional $(\mu = 0.1)$ contact problems are considered.

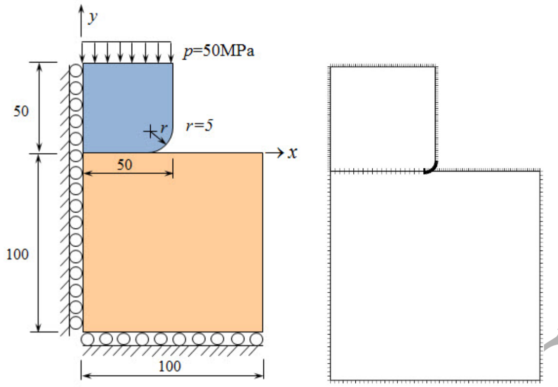

(a) Computational model (b) Computational mesh

Figure 12: A flat rounded punch on a foundation

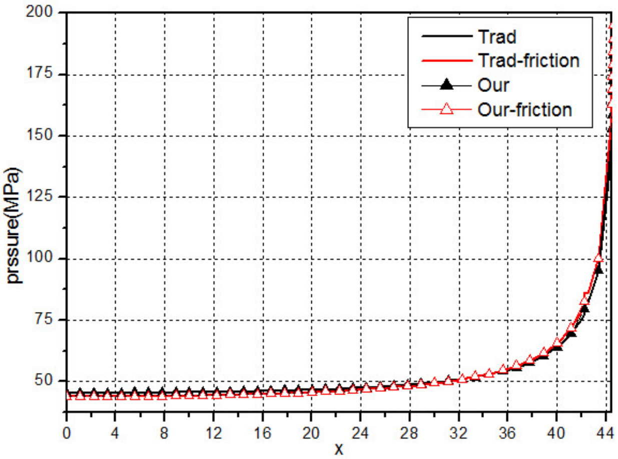

Figure 13: Contact pressure for frictionless and frictional contact, $0 < x < 44.5$

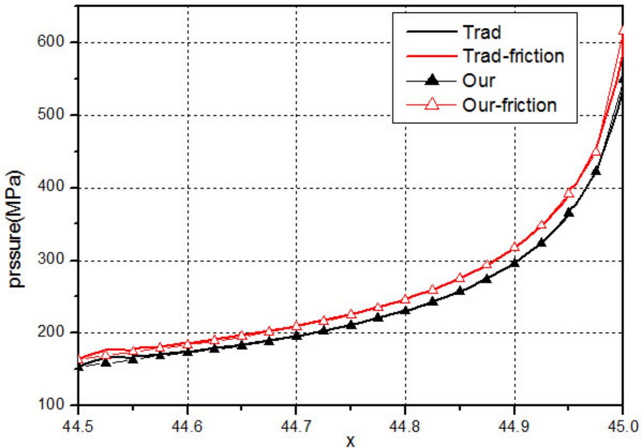

Figure 14: Contact pressure for frictionless and frictional contact, $44.5 < x < 45$

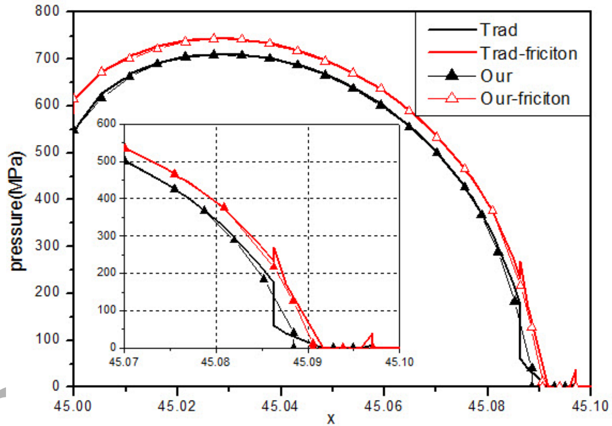

Figure 15: Contact pressure for frictionless and frictional contact, $45 < x < 45.10$

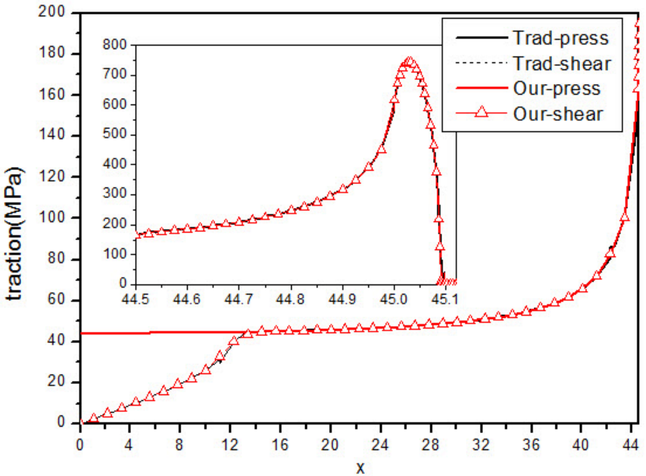

Figure 16: Contact pressure and shear stress for frictional contact ($\mu = 0.1$)

The contact pressure distributions for frictionless and frictional ($\mu = 0.1$) are shown in Figures 13 to 15. The pressure curves in the three figures correspond to the pressure in different areas. The 'Trad' and 'Trad-friction' labels denote the pressure found using traditional discontinuous quadratic elements for frictionless and frictional contact, respectively. The 'Our' and 'Our-friction' labels denote the pressure found using our proposed approach for frictionless and frictional contact, respectively. From the three figures, it can be seen that the result of the proposed approach using S1 elements is almost consistent with that of traditional discontinuous quadratic element. In addition, the pressure oscillations only occur in traditional discontinuous quadratic element, rather than in S1 element, as shown in Figure 15.

In Figure 16, the pressure and shear stress distributions for $\mu = 0.1$ are shown. The 'Trad-press' and 'Trad-shear' labels denote the pressure and shear stress for traditional discontinuous quadratic elements, respectively. The 'Our-press' and 'Our-shear' labels denote the pressure and shear stress in our proposed approach. The shear stress in the Figure has been divided by the frictional coefficient μ. This Figure again shows a good similarity between the results of the proposed approach and those of traditional discontinuous quadratic elements.

This study further demonstrates the ability of the S1 element to achieve an accuracy comparable to that obtained by the traditional discontinuous quadratic element. Meanwhile, it also demonstrates that the pressure oscillations near the contact boundary can be treated in our method.

5.3. Multi-contact zone problem

A multi-contact zone frictional contact problem is shown in Figure 17. Contact takes place over three separate contact zones between the punch and the foundation. For convenience, the three contact zones are called the left, middle and right contact zone. The curved edge of the upper region (the punch) is modelled using five arcs of radius $r = 5$. The material parameters of the punch and the foundation are equal, both having Young's modulus $E = 2000$ and Poisson's ratio $\nu = 0.3$. The frictional coefficient $\mu = 0.2$. The results using traditional discontinuous quadratic elements are used for comparison, and the S1 element in DiBFM is adopted. The initial number of elements in both methods is equal. To obtain a good contact pressure, a fine mesh is used in the contact zones $(-2.19 < x < 3.81)$, $(-14.19 < x < 15.81)$ and $(-26.19 < x < 27.81)$. Each contact zone has 40 elements. The mesh in the non-contact zone can be seen in Figure 17(b).

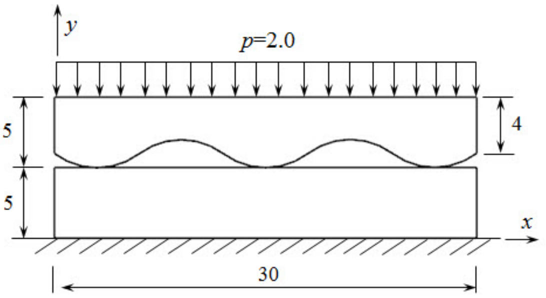

(a) Computational model

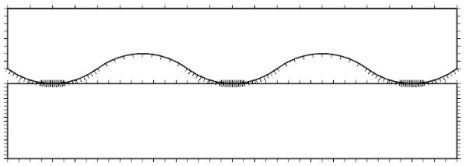

(b) Computational mesh

Figure 17: Multi-contact zone problem

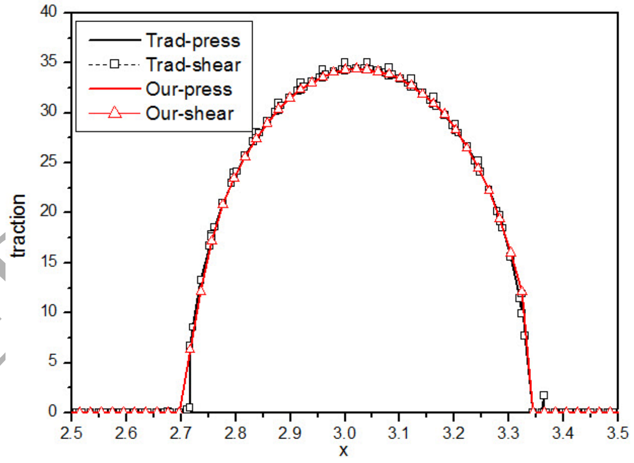

Figure 18: Contact pressure and shear stress for left contact zone

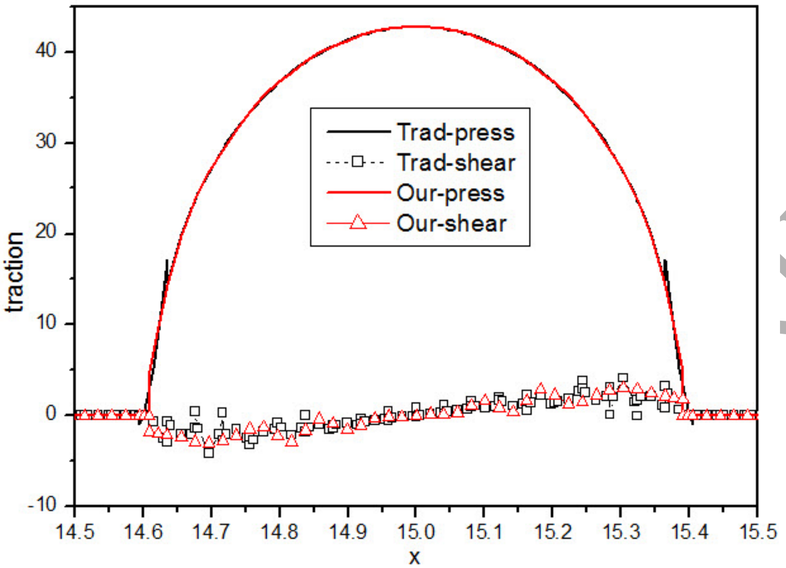

Figure 19: Contact pressure and shear stress for middle contact zone

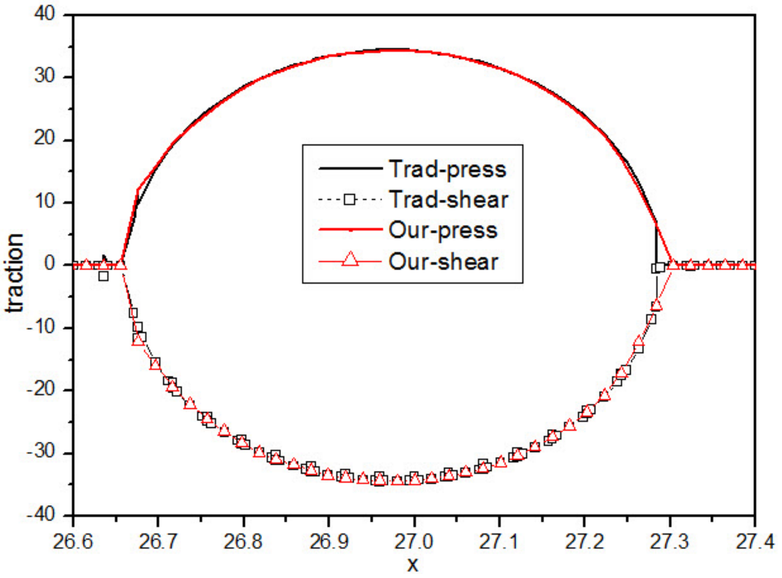

Figure 20: Contact pressure and shear stress for right contact zone

The pressure and shear stress distributions over the three contact zones for

$\mu = 0.2$ are shown in Figures 18 to 20. The 'Trad-press' and 'Trad-shear' labels denote the pressure and shear stress for traditional discontinuous quadratic elements, respectively. The 'Our-press' and 'Our-shear' labels denote the pressure and shear stress for the S1 element in our solution approach. The shear stress in the Figures has been divided by the frictional coefficient μ. It can be seen that the result of the S1 element in the proposed approach is almost coincident with that of the traditional discontinuous quadratic element. Besides, no pressure oscillations occur near the contact boundary in our method. These confirm the conclusions drawn from the first two examples.

6. Conclusions

A solution approach based on the dual interpolation boundary face method (DiBFM) has been proposed for 2D frictionless and frictional contact problems. The solution approach is divided into the outer and inner iteration loops. The size of the contact zone is determined in the outer iteration, while in the inner iteration the contact state (sticking or sliding) is determined; the inner loop is only performed for frictional contact problems. To approximate the discontinuous pressure that arises in some classes of contact problem, a contact boundary detection method has been given, and its validity has been demonstrated by numerical examples. All presented numerical examples, without and with friction, have demonstrated that the S1 element in the proposed approach can achieve the accuracy obtained by traditional discontinuous quadratic boundary elements. In addition, since the S1 element is a continuous element and the contact boundary is detected, the pressure oscillations near the contact boundary can be treated in the proposed approach.

Acknowledgements

This work was supported by National Science Foundation of China under grant number 11772125 and 11472102.

References

References

[1] J. Zhang, W. Lin, Y. Dong, A double-layer interpolation method for implementation of BEM analysis of problems in potential theory, Applied Mathematical Modelling 51 (2017) 250–269.

[2] J. Zhang, W. Lin, Y. Dong, A dual interpolation boundary face method for elasticity problems, European Journal of Mechanics-A/Solids 73 (2019) 500–511.

[3] J. Zhang, L. Han, W. Lin, Y. Dong, A new implementation of BEM by an expanding element interpolation method, Engineering Analysis with Boundary Elements 78 (2017) 1–7.

[4] J. Zhang, Y. Zhong, Y. Dong, Expanding element interpolation method for analysis of thin-walled structures, Engineering Analysis with Boundary Elements 86 (2018) 82–88.

[5] J. Zhang, X. Qin, X. Han, G. Li, A boundary face method for potential problems in three dimensions, International Journal for Numerical Methods in Engineering 80 (2009) 320–337.

[6] P. Bussetta, D. Marceau, J. Ponthot, The adapted augmented Lagrangian method: a new method for the resolution of the mechanical frictional contact problem, Computational Mechanics 49 (2012) 259–275.

[7] T. Cichosz, M. Bischoff, Consistent treatment of boundaries with mortar contact formulations using dual Lagrange multipliers, Computer Methods in Applied Mechanics and Engineering 200 (2011) 1317–1332.

[8] M. Matzen, T. Cichosz, M. Bischoff, A point to segment contact formulation for isogeometric, NURBS based finite elements, Computer Methods in Applied Mechanics and Engineering 255 (2013) 27–39.

[9] D. Franke, A. Düster, V. Nübel, E. Rank, A comparison of the h-, p-, hp-, and rp-version of the FEM for the solution of the 2D Hertzian contact problem, Computational Mechanics 45 (2010) 513–522.

[10] M. Stadler, G. Holzapfel, Subdivision schemes for smooth contact surfaces of arbitrary mesh topology in 3D, International Journal for Numerical Methods in Engineering 60 (2004) 1161–1195.

[11] D. Franke, E. Rank, A. Duester, Computational contact mechanics based on the rp-version of the finite element method, International Journal of Computational Methods 8 (2011) 493–512.

[12] C. Oysu, Finite element and boundary element contact stress analysis with remeshing technique, Applied Mathematical Modelling 31 (2007) 2744–2753.

[13] T. Duong, R. Sauer, An accurate quadrature technique for the contact boundary in 3D finite element computations, Computational Mechanics 55 (2015) 145–166.

[14] J. Kim, S. Youn, Isogeometric contact analysis using mortar method, International Journal for Numerical Methods in Engineering 89 (2012) 1559–1581.

[15] P. Lancaster, K. Salkauskas, Surface generated by moving least squares methods, Mathematics of Computation 37 (1981) 141–158.

[16] C. Brebbia, J. Telles, L. Wrobel, Boundary element techniques, Springer-Verlag, 1984.

[17] F. Paris, J. Garrido, An incremental procedure for friction contact problems with the boundary element method, Engineering Analysis with Boundary Elements 6 (1989) 202–213.

[18] O. Olukoko, A. Becker, R. Fenner, A new boundary element approach for contact problems with friction, International Journal for Numerical Methods in Engineering 36 (1993) 2625–2642.

[19] C. Dong, Some basic aspects on the boundary element methods of elastoplasticity and their applications on contact problems, PhD thesis, Tsinghua University, 1992.

[20] B. Keum, Y. Liu, Analysis of 3-D frictional contact mechanics problems by a boundary element method, Tsinghua Science and Technology 10 (2005) 16–29.

[21] X. Shu, J. Zhang, L. Han, Y. Dong, A surface-to-surface scheme for 3D contact problems by boundary face method, Engineering Analysis with Boundary Elements 70 (2016) 23–30.

[22] K. Johnson, Contact Mechanics, Cambridge University Press, 1985.

[23] A. Blázquez, F. Paris, Effect of numerical artificial corners appearing when using BEM on contact stresses, Engineering Analysis with Boundary Elements 35 (2011) 1029–1037.